Applied Ocean Research 170 (2026) 105064

Contents lists available at ScienceDirect

Applied Ocean Research

journal homepage: www.elsevier.com/locate/apor

Research paper

Investigation of added resistance in regular waves: A numerical study of the influence of leeway angle

Burak Göksu [a,*], Suraj Garad [b], Stefano Pandini [c], Edoardo Sirolla [c], Robert Palin [c], Nicholas Townsend [b], Tahsin Tezdogan [b]

[a] Department of Marine Engineering, Maritime Faculty, Zonguldak Bulent Ecevit University, Zonguldak, Turkey
[b] Department of Civil, Maritime and Environmental Engineering, School of Engineering, Faculty of Engineering and Physical Science, University of Southampton, UK
[c] Spaera Ltd, London, UK

ARTICLE INFO

Keywords:
Added wave resistance
Computational fluid dynamics (CFD)
Leeway angle
Ship resistance
Wind-assisted propulsion system (WAPS)

ABSTRACT

This study investigates the combined effect of a ship's leeway angle and regular waves on the added wave resistance of a general cargo vessel, which is a key factor in energy efficiency. Computational Fluid Dynamics (CFD) simulations are performed on a vessel model at leeway angles ranging from 0° to 10°, across a range of regular head wave frequencies and two Froude numbers (0.194 and 0.246). The CFD results are compared with experimental data, showing an average difference of 5.65% under regular wave conditions and 1.63% under calm water conditions. The results indicate that increasing the leeway angle consistently increases the total resistance in both calm water and wave conditions. The added wave resistance coefficient (σ_{AW}) increases markedly with leeway angle, particularly at a wavelength ratio (λ/Lwl) of approximately 1.6. The zeroth-order harmonic, corresponding to the mean value of the heave motion, is also strongly affected by leeway, whereas the influence of leeway on the first-order harmonics, representing the oscillation amplitudes of pitch and heave motions, is relatively small. The results further demonstrate that the combined action of leeway and waves leads to an increase in added resistance that exceeds the linear superposition of leeway-induced resistance and wave-induced resistance considered separately.

1. Introduction

Increased hydrodynamic resistance has a substantial impact on ship energy efficiency, especially in marine transport, where fuel consumption and greenhouse gas emissions are major problems. To address these concerns, the International Maritime Organization (IMO) has enacted regulations such as the Energy Efficiency Design Index (EEDI), the Energy Efficiency Existing Ship Index (EEXI), and the Ship Energy Efficiency Management Plan (SEEMP), which encourage energy-efficient ship designs and operations (IMO, 2023). It is therefore crucial to comprehend the implications of added resistance, which are directly associated with greenhouse gas emissions and fuel consumption, in order to comply with these regulations.

During the navigation of a vessel through wave conditions, there is an increase in resistance that may account for 15% to 30% of the total resistance (Tezdogan et al., 2015). This observed rise in resistance requires an increase in propulsion power to maintain speed, resulting in high-level fuel consumption. Degiuli et al. (2019) emphasized the significant role of added resistance in waves on increased fuel expenses and CO_2 emissions. They highlighted that precise prediction is essential for improving ship efficiency and reducing environmental consequences. This correlation is especially significant in adverse weather conditions, where the energy needed to counteract this resistance can increase significantly (Jimenez et al., 2022). The reason for this is that the interaction between wave conditions and added resistance is complex, shaped by factors including the ship's hull design, mass properties, and specific environmental conditions (Chen et al., 2018; Lee et al., 2022). In addition to that increasing wavelength typically results in a significant rise in added resistance (Lee et al., 2022; Martić et al., 2020). Furthermore, the added resistance is greatly affected by the ratio of the wavelength (λ) to the waterline length (L_{WL}) of the vessel. Different types of motion result in distinct peaks in the added resistance observed at particular frequencies. Head seas also generally result in greater added resistance when compared to following and beam seas (Cepowski, 2024;

* Corresponding author.
E-mail addresses: burakgoksu@beun.edu.tr (B. Göksu), s.garad@soton.ac.uk (S. Garad), stefano.pandini@spaera.eco (S. Pandini), edoardo.sirolla@spaera.eco (E. Sirolla), rob.palin@spaera.eco (R. Palin), n.c.townsend@soton.ac.uk (N. Townsend), t.tezdogan@soton.ac.uk (T. Tezdogan).

https://doi.org/10.1016/j.apor.2026.105064
Received 23 December 2025; Received in revised form 3 March 2026; Accepted 8 April 2026
Available online 16 April 2026

Kim et al., 2017). One of the reasons could be that the impact of the hull form above the waterline on added resistance in waves fluctuates with wave height (Jawa and Munehiko, 2023).

In the context of energy efficiency of ships, wind-assisted systems have become a crucial element in the transition towards sustainable maritime propulsion. The integration of wind energy into propulsion systems, commonly known as Wind-Assisted Propulsion Systems (WAPS), utilizes the natural force of wind to enhance conventional fuel-based propulsion techniques, consequently reducing dependence on fossil fuels and minimizing environmental impacts (Inal et al., 2022; Pan et al., 2021). Additionally, numerous studies emphasize the potential of wind-assisted systems to significantly decrease emissions, demonstrating their effectiveness in this regard (Cairns et al., 2021; Julià et al., 2020; Liu et al., 2024).

On the other hand, WAPS reduce fuel consumption by generating forward thrust, they also produce considerable lateral forces that must be balanced by the ship, causing the vessel to sail at a non-zero leeway angle. This leeway angle – defined as the angle between the ship's heading and its actual course through the water – has been shown to increase calm water resistance (Göksu et al., 2025). It is therefore a key parameter in assessing the total resistance experienced by a vessel equipped with WAPS. When navigating in waves, the leeway angle may further increase due to lateral forces induced by both the waves and the wind acting on the WAPS. This alters the effective hull configuration exposed to incoming waves, potentially changing the resulting resistance. A larger leeway angle can significantly alter the area where the ship hull encounters the water and the surrounding flow patterns, leading to higher frictional resistance, which, in turn, may exacerbate the added resistance due to waves (Cepowski, 2024; Tezdogan et al., 2015). Numerical simulations have shown that the leeway angle has a substantial effect on a ship's motion responses and resistance characteristics, particularly in head seas where waves directly oppose forward motion (Kim et al., 2017; Seo et al., 2017). Saydam et al. (2022) concluded that a leeway angle greater than 5° has a substantial effect on total resistance. Zhang et al. (2024) reported a 30% increase in total resistance at a 10° leeway angle. However, a critical knowledge gap remains regarding in how this leeway-induced flow interacts with incident waves and influences the added resistance due to waves.

Besides experimental techniques, fluid dynamic simulations have played a crucial role in evaluating the performance of various devices in WAPS applications. Such simulations provide valuable insights into how different configurations can maximise the benefits of wind energy across a range of sea states and wave conditions (Khan et al., 2021; Talluri et al., 2016). Computational fluid dynamics (CFD) methods have proven to be powerful tools for predicting the complex motions of vessels in waves. For example, Zhang et al. (2024) compared experimental (EFD) and numerical findings to support the reliability of the CFD results and verified the 10-degree static drift results by employing a minus 10-degree drift angle in CFD simulations. Additionally, total drag coefficient differences varied from −1.2% to −2.6% between CFD and EFD results depending on the grid resolution, and it should be noted that these findings are limited to the specific calm water and drift conditions investigated in their study. The integration of CFD in the evaluation of WAPS signifies substantial progression in maritime engineering. Such methodologies enable detailed assessment of vessel performance under diverse maritime conditions, offering valuable insights into the effectiveness of different hull configurations in reducing hydrodynamic resistance (Söding et al., 2014; Tezdogan et al., 2015). The capacity to model complex interactions among wind, water, and vessel configurations makes CFD a key tool for enhancing ship designs that utilize wind assistance. Recent studies demonstrate the adaptability of CFD in evaluating wind-assisted propulsion. Plessas and Papanikolaou (2024) emphasize the optimization of ship design for wind propulsion, demonstrating how CFD models can simulate the effects of wind on hydrodynamic and aerodynamic properties, thereby enabling design enhancements to improve fuel efficiency and decrease emissions. Čalić et al. (2024) highlight the significance of CFD by utilizing a mathematical model to predict propeller and engine performance under different wind assistance conditions, illustrating how these simulations indicate potential fuel savings on various vessel types. Additionally, Vigna and Figari (2023) employed CFD simulations to assess the efficacy of Flettner rotors in combination with controllable pitch propellers, facilitating a comprehensive understanding of the synergistic operation of these systems to optimize thrust and reduce fuel consumption. Huang et al. (2023) examined the aerodynamic properties of the Flettner rotor by CFD, indicating that optimizing rotor geometry can significantly enhance its efficacy in wind-assisted applications. Moreover, the combination of CFD with other modelling tools, encompassing sophisticated data analysis methodologies, could transform performance evaluations. The integration of CFD with machine learning can improve the predicted accuracy of wind propulsion research, revealing insights that may be hidden in conventional modelling approaches (Guerri et al., 2016). The application of CFD facilitates the comprehensive simulation of fluid dynamics, enabling researchers and engineers to assess the efficacy of various wind propulsion technologies in reducing fuel consumption and emissions in maritime transport (Göksu et al., 2025).

Evaluating the combined impact of leeway angle and regular wave phenomena on added wave resistance is essential for improving vessel operational performance and efficiency. This study provides important insights into the interaction between a vessel's leeway angle - induced by a wind-assisted propulsion system - and the added resistance caused by regular waves, addressing a notable gap in the literature. Unlike previous studies that have examined these effects in isolation, this research aims to quantify their combined influence under controlled experimental and numerical conditions. By analysing this complex relationship, naval architects can optimise hull designs and propulsion systems to reduce resistance, thereby by improving fuel efficiency and lowering operational costs. Furthermore, such understanding enables ship operators to make well-informed decisions on route planning, speed optimization, and fuel management, contributing to a more sustainable and economically viable maritime sector.

This study addresses this gap by examining the combined effect of leeway angle and regular waves on a ship's hydrodynamic performance. Building upon the foundation laid in the preceding sections, it presents a rigorous investigation into resistance calculations for a general cargo ship model. A CFD approach was employed to explore the resistance components in detail. The methodology section outlines the specific procedures and CFD parameters used, while the Results and Discussion section outlines the core findings in relation to existing literature, highlighting their broader implications. Finally, the conclusion synthesizes these elements, emphasizing the study's contributions and suggesting potential directions for future research to further refine and expand the knowledge presented.

2. Research outline and limitations

This study investigated the total resistance of a case vessel using a 1:32 scale model for both CFD analysis and EFD tests at the University of Southampton's Boldrewood Towing Tank. The full-scale vessel's speeds (11 knots operational, 14 knots maximum) correspond to model speeds of 1 m/s and 1.273 m/s. The primary aim was to determine total resistance under calm water and regular head wave conditions using CFD. In the CFD analyses, a fixed wave amplitude of 0.015 m was used across 11 distinct wave frequencies, and five leeway angles (0° to 10°) were tested at both model speeds. EFD tests were crucial for refining CFD parameters and validating results; they were performed only at the operational speed of 1 m/s and 0° leeway, covering a subset of 5 wave frequencies (0.700, 0.732, 0.768, 0.858 and 1.086 Hz) to provide comparative data for the CFD results. Table 1 serves to introduce the summary of the CFD analysis and EFD test conditions.

This investigation establishes a foundational analysis of coupled hydrodynamic effects by focusing on the interaction between leeway

Table 1
Summary of CFD and EFD test conditions.

Parameters	Details
Model scale	1:32
Full-scale speeds	11 knots (Operational) and 14 knots (Maximum)
Model-scale speeds	1 m/s (Operational) and 1.273 m/s (Maximum)
Fluid conditions	Calm Water and Regular Wave
Leeway angles	0°, 2.5°, 5°, 7.5°, 10°
Wave frequencies	0.450, 0.500, 0.550, 0.600, 0.650, 0.700, 0.732, 0.750, 0.768, 0.858, 1.086 Hz

angle and regular head waves at a fixed 0° rudder angle. To isolate the interaction effects between rudder and leeway angle, this investigation focuses on controlled conditions involving regular head waves and a fixed rudder angle of 0°, establishing a fundamental baseline before extending the analysis to irregular, multidirectional seas and dynamic steering scenarios.

This research aims to replicate towing tank tests within a computational framework. Consequently, although the leeway angle phenomenon analysed in this study shares certain similarities with oblique sea conditions, it does not present an identical scenario. Within the adopted CFD methodology, changing the wave encounter angle can influence ship motions through wave reflection from the numerical domain boundaries. In contrast, introducing a leeway angle generates a condition analogous to that encountered in wind-assisted propulsion, as it produces a persistent modification of the viscous resistance and pressure distribution around the ship. This comprehensive evaluation of coupled effects advances vessel design, enhances operational efficiency, and supports safer shipping practices.

In this study, only heave and pitch movements were allowed to isolate the fundamental vertical responses in the head waves, while roll movement was constrained. Nevertheless, asymmetric flow induced by leeway was observed to generate a residual roll moment (K'), particularly at higher leeway angles such as 10° Allowing roll motion could alter the instantaneous waterline geometry and introduce secondary effects on wave added resistance. While the present results remain valid within this modeling framework, future studies should consider releasing roll motion to provide a more comprehensive assessment of vessel performance under leeway conditions.

3. Research methodology

This section presents the methodology used to assess the resistance of the case ship through the Computational Fluid Dynamics approach. The CFD analyses were supported by towing tank experimental data (Garad et al., 2024) to enhance the accuracy and reliability of the numerical method's results. By integrating the strengths of both numerical and experimental techniques, an efficient framework for evaluating ship resistance performance was established. To ensure consistency and contextual clarity, a fixed rudder angle of 0° was maintained throughout the simulations. The following subsections detail the key methodologies and technical procedures employed, including the CFD configuration, verification process, and the extrapolation of model-scale resistance results to full-scale conditions.

3.1. Definition of the case ship

Table 2 presents the particulars of the full-scale vessel and its corresponding 1:32 scale model used in this study.

The ship hull and the coordinate system used in this investigation are shown in Fig. 1. The coordinate system was defined according to the right-hand rule. The ship's keel was aligned with the x-axis at an elevation zero, with the bow pointing in the positive x-direction. The port side was oriented towards the +y direction, while the +z direction extended vertically from the keel to the deck, opposite to the direction of gravitational force.

Table 2
The particulars of the case ship and the model.

Particulars	Values		Units
	Ship	Model	
Displacement volume	5865	0.179	m^3
Draught amidships (T)	5.45	0.170	m
Waterline length (Lwl)	87.10	2.722	m
Beam maximum (B)	15.20	0.475	m
Wetted area	2049	2.001	m^2
Prismatic coefficient (C_p)	0.828		–
Block coefficient (C_b)	0.826		–
Maximum section area coefficient (C_m)	0.997		–

3.2. Dimensionless parameters

For each CFD simulation case - defined by model speed, leeway angle, and incident wave conditions - the model ship's motions, along with the rolling (M_x) and yawing (M_z) moments, were obtained. These variables were recorded as time histories, similar to the resistance measurements, enabling detailed characterisation of the hull's hydrodynamic behaviour. The non-dimensional rolling and yawing moment coefficients, K' and N' respectively, are defined in Eqs. (1 and 2) (ITTC, 2024).

$$K' = \frac{M_x}{(1/2)\rho U_C^2 TLB} \tag{1}$$

$$N' = \frac{M_z}{(1/2)\rho U_C^2 TL^2} \tag{2}$$

where, U_C is the current speed (equivalent to the model's forward velocity in the towing tank) [m/s], ρ is the density of fluid [kg/m^3], B is the beam [m], L represents the characteristic length (ship or model) [m], and T represents the draught [m].

3.3. Calm water resistance

The International Towing Tank Conference (ITTC) formulates the technique for assessing ship resistance by examining its components and describing the necessary procedures for this computation. It also indicated that vessels with design speeds corresponding to Fr lower than 0.45 are typically described as conventional displacement ships. The total resistance coefficient (C_T), described in Eq. (3), for vessels is a dimensionless parameter that signifies the total resistance of a ship to navigate through water. It is defined as the ratio of the total resistance (R_T) [N] to the dynamic pressure of the fluid, multiplied by the wetted surface area (S) [m^2] of the vessel's hull (ITTC, 2021a).

$$C_T = \frac{R_T}{\frac{1}{2}\rho S V^2} \tag{3}$$

$$C_T = C_V + C_W \tag{4}$$

where, C_V represents viscous resistance coefficient and C_W is for wave-making resistance coefficient.

$$C_V = C_F(1+k) \tag{5}$$

The form factor approach was employed to determine the total resistance. The Hughes formulation, given in Eq. (6), was used to evaluate the frictional resistance coefficient (C_F), as it is well suited to the form factor method by providing a strictly two-dimensional friction baseline. Using the Holtrop and Mennen (1982) formulation, the vessel form factor (1 + k) was determined to be 1.334. To assess the reliability of this relatively high value, a high-fidelity CFD double-body simulation was conducted in a related study by the authors on the same hull form

Fig. 1. The hull model of the case ship and the global coordinate system for CFD analysis.

(Göksu et al., 2025). That investigation yielded a form factor of 1.33, demonstrating close agreement with the empirical estimate. This consistency supports the validity of the viscous resistance components adopted in the present added resistance analysis.

$$C_F = \frac{0.066}{\left(\log_{10} Re - 2.03\right)^2} \tag{6}$$

The C_F parameters are calculated based on the Reynolds number and are determined independently for both the model and ship scales. The C_{TM} value is determined from the R_{TM} value derived from the model-scale analysis results. Subsequently, the C_{VM} and C_W values are derived by computing the Re at the model scale velocity. As the wave-making coefficient, influenced by the hull's shape, remains constant throughout both model and ship scales, the total resistance coefficient of the vessel (C_{TS}) is determined using C_{FS} derived at full-scale.

3.4. Added wave resistance

Wave-induced resistance, known as added wave resistance, increases resistance compared to calm water because the vessel experiences six degrees of freedom of motion and direct hull-wave interactions. This resistance fluctuates with the vessel's movement on wave slopes and changing water pressures, depending on the wave's frequency and amplitude, and it is typically calculated as a time-averaged value.

The added resistance due to waves (R_{AW}) is calculated, given in Eq. (7), by subtracting the calm water resistance ($R_{T,calm}$) from the average drag force value in waves ($R_{T,wave}$), and defined as non-dimensional form in Eq. (8).

$$R_{AW} = R_{T,wave} - R_{T,calm} \tag{7}$$

$$\sigma_{AW} = \frac{R_{AW}}{\rho g \zeta_a^2 B_{wl}^2 / L} \tag{8}$$

where,

ζ_a: is the harmonic amplitudes of the incident wave profile [m],
B_{wl}: is the width of the hull at waterline [m]

The added wave resistance coefficient (σ_{AW}) enables the comparison of wave resistance performance among various vessels and enables the extrapolation of model test results to full-scale ships.

3.5. Computational fluid dynamics methodology

The section explains that solving the Reynolds-Averaged Navier-Stokes (RANS) equations is a key numerical method in ship hydrodynamics, used to model turbulent flows by decomposing flow variables into mean and fluctuating components and using time-averaged quantities. While standard RANS is used to model turbulent flows, the Unsteady RANS (URANS) method offers improved accuracy by specifically capturing the temporal fluctuations of these flows. In this study, the RANS equations were solved using Star-CCM+ (version 18.04.008), a commercial CFD software developed by (CD-Adapco, 2023).

3.5.1. Computational domain and boundary conditions

The boundary conditions for the CFD simulations were defined based on the cross section of the Boldrewood Towing Tank at the University of Southampton, where the experimental tests were conducted. The computational domain measured 16 m in length, 6 m in width, and 3.5 m in water depth, with an additional 2 m air layer above the waterline. To replicate the experimental setup, the sidewalls and bottom surface of the domain were treated as no-slip wall boundaries (grey surfaces). The region downstream of the hull was specified as a pressure outlet (red surface) to allow for the development of the wake generated by the model. The upstream boundary and the free surface above the air layer (green surfaces) were defined as velocity inlets to establish the incoming flow conditions. Additionally, a no-slip wall boundary condition was used on the ship hull surface (black surfaces) to accurately model the viscous resistance and boundary layer features. Fig. 2 shows the hull model within the overset domain (yellow surfaces), together with the surrounding background domain.

The fluid flow arriving at the overset mesh region passes through a distance of $\sim 1Lwl$. Upon exiting, it covers a distance of $\sim 3.5Lwl$, contributing to the formation of the ship wake region. The dimensions of the overset mesh region are characterized by a height that is ~2.3 times the depth of the model, a length is $\sim 1.3Lwl$, and a width that is $\sim 2.1B$ for a 2.5° leeway angle. The width of the overset region depends on the leeway angle, a necessary adjustment to maintain full coverage of the vessel's hull.

3.5.2. Mesh generation

The trimmer mesh in Star-CCM+ is well-suited for representing complex geometries. In this study, the surface remesher tool was employed to create a customised mesh configuration. Particular attention was given to smoothing mesh elements in regions where water and air interact—especially around the hull and free surface—to improve accuracy. Several volumetric refinement zones of different sizes were introduced: three were applied to capture the free surface with high fidelity, while two were used to resolve hull motions relative to the overset mesh boundaries, both internally and externally. This refinement strategy enabled a more detailed representation of free-surface wave conditions, thereby improving the prediction of vessel motions. Fig. 3 illustrates the mesh configuration, which comprised approximately 14 million elements for the 0° leeway angle case.

The mesh was created in accordance with the ITTC (2011) requirements for ship CFD applications that simulate ship motions in waves. These standards demand a minimum of 80 cells per wavelength and 10 cells per wave height on the free surface. On the other hand, the overset mesh serves as a numerical equivalent to the moving fluid region surrounding the hull, facilitating the analysis of vessel motions under various wave conditions.

3.5.3. Physics modelling

The CFD solver employed the finite volume method (FVM) in combination with a high-resolution interface-capturing (HRIC) scheme to accurately resolve the free surface and complex flow patterns around the hull. To simulate the ship's motions, Star-CCM+'s overset mesh capability was used to generate a high-fidelity mesh around the model, embedded within a finer region of the static background domain. As the fluid evolves within the computational domain, the overset mesh dynamically updates its translation and orientation relative to the background mesh, enabling precise tracking of the vessel's motion and accurate resolution of near-field flow features. This overset mesh approach is widely applied in hydrodynamic and aerodynamic studies

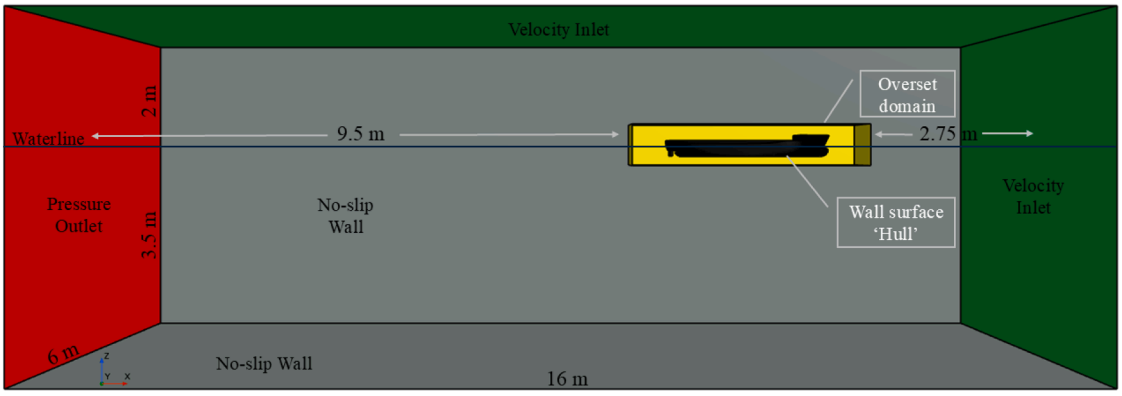

Fig. 2. Boundary conditions and fluid domain for regular wave analysis.

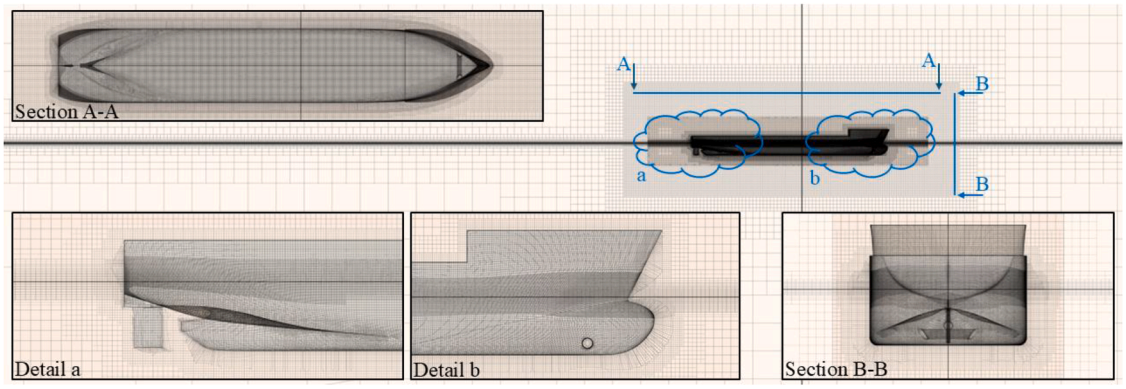

Fig. 3. Details of the generated mesh configuration for 0° leeway angle.

due to its effectiveness in handling complex geometries, modelling moving bodies, and enhancing overall simulation accuracy (Carrica et al., 2011; Kim et al., 2021).

A complex multiphase flow around the ship model was simulated using the Volume of Fluid (VOF) approach and the K-ε Realizable turbulence model. This robust combination was ideal for modelling complex water-air interactions, where interfacial dynamics and turbulent mixing must be accurately represented. VOF accurately tracks wave production, breaking, and air inlet on the free surface (water-air interface). The K-ε Realizable turbulence model improves upon the standard K-ε model by more accurately predicting turbulent stresses, which is especially important in ship hydrodynamics where pressure gradients and flow separation are dominant.

Calm water resistance analyses were performed to represent a reference scenario to compare the hydrodynamic performance under regular wave conditions. The following fluid properties were used to define the characteristics of the fluids: water with a density of 999.1026 kg/m^3 and a dynamic viscosity of 0.001138 *Pa.s*, and air with a density of 1.18415 kg/m^3 and a dynamic viscosity of $1.855x10^{-5}$ *Pa.s*. These values are crucial input parameters for the simulation, directly influencing the forces and moments acting on the model.

Finally, to assess the hull's dynamic behaviour beyond resistance, the Dynamic Fluid–Body Interaction (DFBI) model in Star-CCM+ was employed to capture the heave and pitch motions (2-DOF). These degrees of freedom were selected as they represent the dominant responses of the hull under head-wave conditions, while surge, sway, roll, and yaw were constrained to isolate the primary vertical motions.

3.5.4. Time step and y^+ value selection

Accurate selection of time step and y^+ values is critical for CFD simulations, particularly in turbulence modelling and wall-bounded flows such as ship resistance analysis. These parameters directly influence simulation accuracy, stability, and computational efficiency, affecting both flow field resolution and the prediction of forces and moments. In transient flow analyses, quasi-static assumptions are often applied, where the system is considered to change slowly enough to be approximated as a sequence of steady states. This governs the choice of time step and temporal resolution required to capture the relevant physical phenomena without incurring excessive computational cost. In the present ship resistance analysis, performed at a model velocity of 1 m/s ($Fr = 0.194$) and a wave frequency of 0.450 Hz (encounter wave period of 1.721 s), a time step of 0.0067 s was adopted. Together with second-order discretisation schemes and a target $y^+ \approx 30$, these settings ensured the fidelity of the turbulence model and the overall accuracy of the simulation.

In calm-water simulations, a commonly applied guideline for the maximum time step is $0.0035L/U$, where L is the model length [m] and U is the model speed [m/s]. This criterion provides adequate temporal resolution to capture the principal flow features. However, for the regular wave analyses conducted in this study, a more stringent approach was adopted: the time step was set to the encounter wave period divided by 256. This refinement was necessary to accurately resolve the rapidly varying flow field generated by wave–hull interactions.

The ITTC (2014) guidelines provide recommendations for the non-dimensional wall distance of the first grid point from the wall, and Fig. 4 represents the y^+ values for leeway angles of 0°, 2.5°, 5°, 7.5°, and 10° at a *Fr* of 0.194 and a 0.450 Hz wave frequency. For accurate CFD simulations of the ship's hull, capturing the boundary layer's complex details and modelling turbulence requires an appropriate and uniformly distributed y^+ value. This study's numerical analysis carefully verified that a consistent y^+ value, close to 30, was reached across all simulated speed situations, assuring compliance with these standards and ensuring

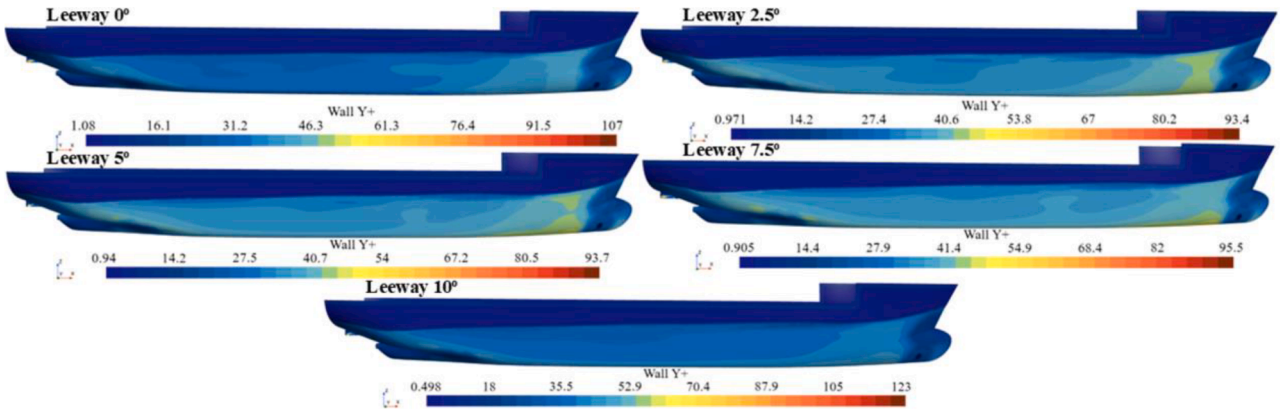

Fig. 4. Distribution of y^+ values on the hull at a *Fr* of 0.194 and a wave frequency of 0.450 Hz.

the results' dependability. This meticulous attention to y^+ values resolves near-wall flow, improving skin friction and total resistance predictions. The uniform application provides confidence when comparing simulation results internally or to other investigations.

Friction velocity (u^*):

$$u^* = \sqrt{\frac{T_w}{\rho}} \tag{9}$$

Non-dimensional wall velocity (u^+):

$$u^+ = \frac{u}{u^*} \tag{10}$$

Non-dimensional wall distance (y^+):

$$y^+ = \frac{\rho u^*}{\mu} y \tag{11}$$

where, T_w is the skin friction, u is the local velocity, μ is the dynamic viscosity of the fluid, and y is for the wall-normal coordinate.

This study adhered to the general recommendation of maintaining a Courant–Friedrichs–Lewy (CFL) number below 1 to ensure the stability of the numerical simulations (see Table 3). The CFL number is a dimensionless parameter relating flow velocity through a cell to the cell size. While a value below 1 is a common guideline, the specific stability threshold (C_{max}) can vary depending on the analysis, as defined by Eq. (12).

$$\frac{\Delta t|\overline{u}|}{\Delta x} < C_{max} \tag{12}$$

where,

Δt: is for the time step
$\overline{u}$: is for the local velocity
Δx: is for the linear size of the flow direction

Table 3
Numerical solution parameters associated with the CFL number.

V_s [knots]	V_m [m/s]	Wave period T_m [s]	Wave freq. [Hz]	Δt [s]	Δx [m]	CFL number
11 / 14	1 / 1.273	2.222	0.450	0.0067 / 0.0063	0.0125	0.5377 / 0.6447
		2.000	0.500	0.0059 / 0.0055		0.4721 / 0.5633
		1.818	0.550	0.0052 / 0.0049		0.4189 / 0.4976
		1.667	0.600	0.0047 / 0.0044		0.3750 / 0.4435
		1.538	0.650	0.0042 / 0.0039		0.3383 / 0.3984
		1.429	0.700	0.0038 / 0.0035		0.3071 / 0.3603
		1.366	0.732	0.0036 / 0.0033		0.2896 / 0.3389
		1.333	0.750	0.0035 / 0.0032		0.2804 / 0.3277
		1.302	0.768	0.0034 / 0.0031		0.2717 / 0.3171
		1.166	0.858	0.0029 / 0.0027		0.2341 / 0.2715
		0.921	1.086	0.0021 / 0.0019		0.1689 / 0.1932

3.5.5. Regular wave generation

First-order numerical wave generating techniques in CFD, characterised by truncation errors that scale linearly with the discretization step size (Stagonas et al., 2018), offer notable advantages in terms of stability and robustness, particularly in simulations involving complex flow topologies or strong gradients. Their inherent dissipative nature suppresses oscillatory instabilities but also introduces numerical diffusion, which can smooth sharp features and reduce solution accuracy (Gao et al., 2021). To achieve accuracy comparable to higher-order schemes, first-order methods therefore require finer grid resolutions. Nevertheless, their lower computational cost per cell and enhanced stability make them suitable for CFD applications where solution convergence is critical. In wave modelling, first-order linear wave theory provides a simplified framework for generating regular wave conditions, based on the assumptions of small-amplitude waves and deep-water conditions (Klein et al., 2020).

A wave probe was employed to measure the wave elevation at the inlet in each analysis. Fig. 5 depicts the location of the wave probe situated between the inlet and the ship model. Fig. 6 illustrates the latest 40-second record history of wave elevation data according to the global coordinate system (*considering 0 m is the waterline*) at the probe at a *Fr* of 0.194 and a wave frequency of 0.450 Hz at a 2.5° leeway angle.

Utilizing the Fourier Series on a segment of the time series of wave oscillation depicted in Fig. 6, the average of the first harmonic wave amplitudes for the last ten periods of the encounter was determined to be 0.0144 m, which underestimates the actual wave amplitude (0.015 m) by 4.17%. The minor decrease in wave amplitude was deemed acceptable for the existing cell size and time step and was considered adequate for validating wave creation by the current CFD model.

3.6. Verification study

This section describes the verification study undertaken to ensure the numerical accuracy and consistency of the CFD methodology, adhering to ITTC procedures ITTC (2021b). Verification focuses on measuring the discretization error and confirming that the simulation solution is

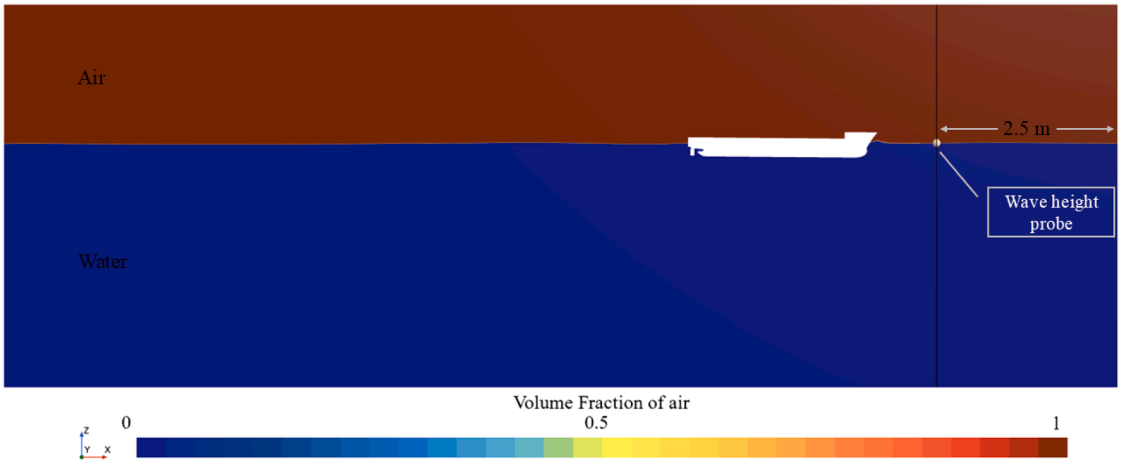

Fig. 5. Position of the numerical wave probe.

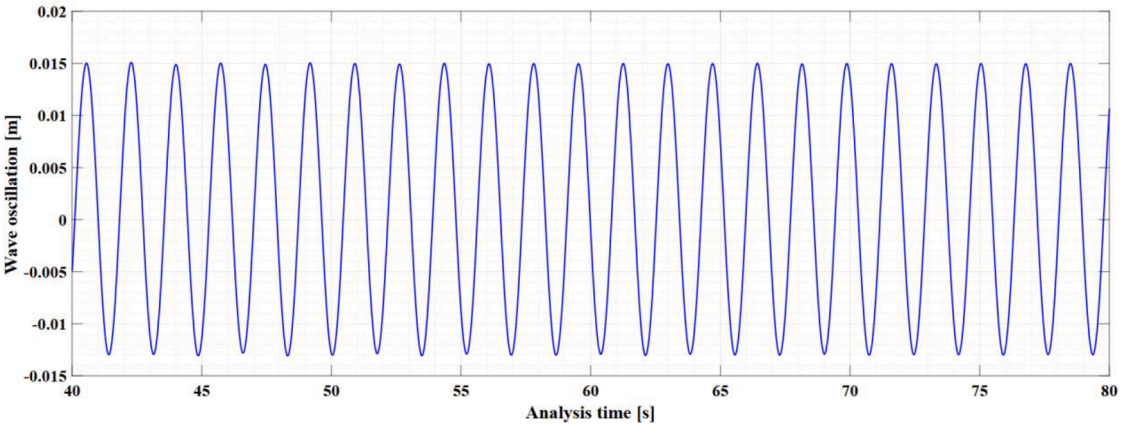

Fig. 6. Wave oscillation history for $Fr = 0.194$ at 2.5° leeway angle and 0.450 Hz wave frequency.

independent of grid resolution. Discretization error arises from approximating continuous equations on a computational grid, meaning finer meshes (smaller grid spacing) should yield solutions closer to the true value. The key to this process is a methodical mesh generation and refinement strategy, which involves creating a sequence of increasingly finer grids (typically using a consistent refinement ratio like 2, $\sqrt{2}$ or $\sqrt[3]{2}$ while maintaining stringent control over mesh quality. The ultimate goal is to balance computational expense with sufficient resolution to capture flow characteristics accurately and ensure the solution is grid-independent.

In this study, the verification analysis was implemented within the CFD methodology by systematically refining the mesh parameters described in Table 4. Additionally, three distinct time steps were established: 0.0052 s, 0.0074 s, and 0.0104 s, facilitating the performance of nine analyses. The notion of base size facilitates the proportional modification of additional parameters, including surface dimensions and boundary layer thickness, in relation to the base value. Adjusting the base size value is sufficient for enhancing or reducing the grid resolution. In this process, the mesh size and boundary layer on the surfaces defining the ship geometry were maintained consistently to generate varied ship hull mesh configurations, leading to analysis results that deviate from the intended objective. The refinement ratio ($\sqrt{2}$) employed for the base mesh size is likewise utilized for the time step values to evaluate the effect of the computation parameters on the results.

The total resistance values for the model ship, operating at a *Fr* of 0.194 with a leeway and rudder angles of 0°, according to the wave frequency of 0.550 Hz, are presented in Table 5.

Fig. 7 was created to improve understanding of the total resistance results associated with the parameters incorporated in the verification study, as the convergence test.

To assess the impact of mesh density on the accuracy of solutions in numerical analyses, the grid convergence index (GCI) is suggested by Celik et al. (2008). In this study, three particular grid resolutions (M1, M2, M3) were utilized to conduct the verification analysis. This method was implemented to guarantee the convergence of the numerical solution. The results concerning solution accuracy were subsequently

Table 4
Grid resolution details for the verification study.

Label	Grid resolution	Base mesh size [m]	Total number of elements
M3	Coarse mesh	0.500	12,727,693
M2	Medium mesh	0.350	13,345,440
M1	Fine mesh	0.250	13,993,170

Table 5
Values of total resistance [N] at model scale for the verification study.

Base mesh sizes [m]	Time steps [s]		
	0.0104	0.0074	0.0052
0.500	6.8641	6.7660	6.7333
0.350	6.7856	6.5372	6.5025
0.250	6.6638	6.4572	6.4374

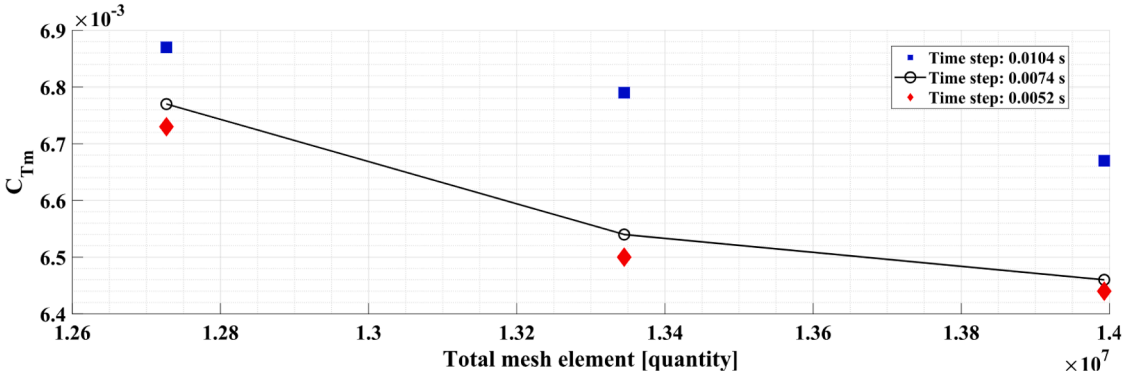

Fig. 7. Total resistance results and mesh element quantities for the convergence test.

determined. By obtaining the previously mentioned solutions, one can determine whether the solution converges or diverges. This is carried out in accordance with the convergence ratio, as shown in Eq. (13) (Celik et al., 2008).

$$R = \varepsilon_{21}/\varepsilon_{32} \tag{13}$$

where, f_1, f_2 *and* f_3 are the total resistance values and difference between medium-fine meshes ($\varepsilon_{21} = f_2 - f_1$), and between coarse-medium meshes ($\varepsilon_{32} = f_3 - f_2$). The convergence conditions defined by the (ITTC, 2021b).

- for $0 < R < 1$; Monotonic convergence,
- for $R < 0$ and $|R| < 1$; Oscillatory convergence,
- for $R > 1$; Divergence.

For the calculation of the order of accuracy (p), Eq. (14) can be used (Celik et al., 2008).

$$p = \frac{1}{\ln r}|\ln|\varepsilon_{32}/\varepsilon_{21}| + q(p)| \tag{14}$$

where, the function $q(p) = 0$ for uniform refinement ratio.

If the refinement ratio is taken non-uniformly, $q(p)$ is calculated by Eq. (15).

$$q(p) = \ln\left(\frac{r_{21}^{p} - s}{r_{32}^{p} - s}\right) \tag{15}$$

where, $s = sign(\varepsilon_{32}/\varepsilon_{21})$, refinement ratio between medium-fine meshes is depicted as r_{21}^{p} and r_{32}^{p} is for between coarse-medium mesh refinement ratio. Then, one can calculate the extrapolated solution is defined by Eq. (16).

$$f_{ext} = (r^{p} f_1 - f_2)/(r^{p} - 1) \tag{16}$$

The grid convergence index, depicted in Eq. (17), provides an estimation of the percentage difference between medium-fine meshes.

$$GCI_{21} = 1.25\left|\frac{f_1 - f_2}{f_1}\right| \Big/ (r^{p} - 1) \tag{17}$$

The results shown in Table 5 indicate that the calculated resistance of the hull is dependent upon the CFD parameters employed, particularly the mesh density and time step size. As the mesh is refined or smaller time steps are employed, the resistance force prediction typically decreases, indicating that the simulations are converging towards a consistent result. This trend was further analysed in Table 6 using a convergence analysis, utilizing data obtained directly from Table 5. The estimated orders of accuracy (p) for both grid and time-step convergence exceeded the theoretical order of the second-order discretization techniques utilized. Eça and Hoekstra (2009) indicate that elevated p values may result in an excessively optimistic (artificially low) GCI. To establish a more cautious and dependable uncertainty constraint, the accuracy order employed in the GCI formulation was restricted to the theoretical value of $p = 2.0$, in alignment with the recommended safety criteria for CFD verification. According to this investigation, the f_{ext} value, was approximated to be between 6.372 and 6.418 Newtons.

Table 6
Verification study results for grid and time step convergence.

	R_t for mesh base size convergence (with monotonic convergence)	R_t for time step convergence (with monotonic convergence)
r	$\sqrt{2}$	$\sqrt{2}$
f_1	6.4374	6.4374
f_2	6.5025	6.4572
f_3	6.7333	6.6638
R	0.282	0.096
p	3.652 (limited as 2.0)	6.767 (limited as 2.0)
f_{ext}	6.372	6.418
GCI_{21}	1.264%	0.384%

Additionally, the GCI was utilized to assess the uncertainty induced by these factors. Despite the conservative adjustment, the identified difference is that the uncertainty related to the mesh size is 1.264%, while the uncertainty associated with the time step size is far lower, at about 0.38%, based on the analysed fine mesh structure. This disparity clearly demonstrates that mesh density currently acts as the most important determinant of numerical accuracy, significantly exceeding the effect of time step size. It can be concluded that when a more accurate resistance estimate is needed, further mesh refinement is required rather than further reducing the time step.

4. Results and discussion

This section presents the CFD analysis results and evaluates their implications for the vessel's resistance characteristics. The main objective is to quantify and understand the added resistance in regular waves under varying operating conditions. To assess the accuracy of the numerical approach, the CFD predictions were first benchmarked against experimental data (Garad et al., 2024). Results are reported in terms of the non-dimensional wavelength (λ/Lwl, the ratio of wavelength to the ship's waterline length), vessel speed (Froude numbers $Fr = 0.194$ and 0.246), and leeway angle ($\beta = 0° - 10°$), focusing on their effects on the added wave resistance coefficient (σ_{AW}). The following subsections first present the benchmarking results, followed by a discussion of the observed parametric trends.

Table 7 compares the total resistance of the case ship, using CFD results from the present study against the EFD data reported by Garad et al. (2024). To improve the clarity and visibility of the values in Table 7, Fig. 8 was generated. The comparison includes calm-water conditions—serving as the baseline resistance at a Froude number of 0.194—as well as regular waves with frequencies ranging from 0.700 Hz

Table 7
Comparison of EFD and CFD values at regular wave and calm water conditions in model scale at $Fr = 0.194$ (for 0° leeway angle).

Wave frequency (ω) [Hz]	Enc. wave period (T_e) [s]	σ_{AW} by EFD	σ_{AW} by CFD	σ_{AW} diff. bet. EFD and CFD	C_{Tm} ($x10^3$) by EFD	C_{Tm} ($x10^3$) by CFD	C_{Tm} diff. bet. EFD and CFD	C_{Tm} by EFD	C_{Tm} by CFD	Diff. bet. EFD and CFD [%]
Regular wave conditions								Calm water conditions		
0.700	0.983	5.848	4.118	−29.58%	6.405	5.943	−7.22%	5.335	5.249	−1.63%
0.732	0.927	6.138	3.443	−43.91%	6.457	5.829	−9.73%			
0.768	0.869	5.339	3.120	−41.57%	6.311	5.774	−8.51%			
0.858	0.749	2.746	2.801	1.99%	5.837	5.721	−2.00%			
1.086	0.540	2.177	2.615	20.10%	5.734	5.689	−0.77%			

Note: EFD analysis results were taken as the reference for deviation calculations.

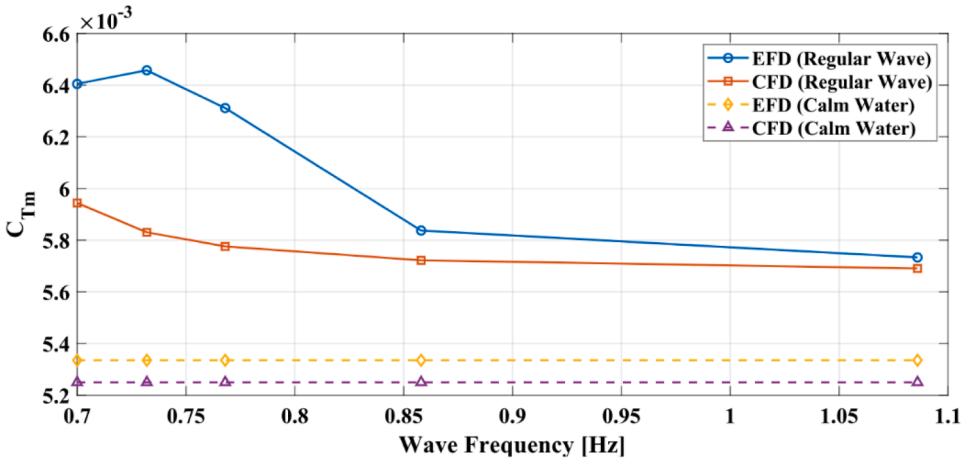

Fig. 8. Results of the EFD and CFD methods under regular wave and calm water conditions at $Fr = 0.194$ (for 0° leeway angle).

to 1.086 Hz. In the regular-wave towing tank tests, sinusoidal waves were applied, while the model ship's forward speed (1 m/s) and wave amplitude (0.015 m) were kept constant.

Table 7 presents a comparison between the available CFD findings and the experimental data (EFD). The mean deviation in the total resistance coefficient (C_{Tm}) remains within acceptable limits, amounting to 1.63% in calm water and 5.65% under regular wave conditions. However, examination of the added wave resistance coefficient (σ_{AW}) reveals that these relatively small differences in total resistance led to more pronounced discrepancies in σ_{AW}, particularly at 0.732 Hz, where a deviation of 43.91% is observed. This behaviour arises from the high sensitivity of the wave amplitude square (ζ_a^2) term in the denominator of the σ_{AW} formulation. Numerical attenuation of the incident wave amplitude is therefore identified as the primary source of this non-linear sensitivity.

To ensure methodological consistency and alignment with current ITTC recommendations, the attenuated wave amplitude measured at the CFD wave probe, 0.0144 m, was used in the calculation of σ_{AW}, instead of the theoretical wave amplitude of 0.015 m. This adjustment led to improved agreement between the CFD and experimental results, particularly at higher wave frequencies, with deviations of 1.99% at 0.858 Hz and 20.10% at 1.086 Hz.

Overall, the discrepancies observed in σ_{AW} can be attributed in part to the pronounced non-linear behaviour of low-frequency waves near resonance conditions, as well as their increased sensitivity to transient reflections, potentially originating from the experimental tank boundaries. Despite these effects, the consistent trend observed across the investigated frequency range and the high level of accuracy in the short-wave regime indicate that the adopted numerical configuration is suitable for analysing the coupled effects of leeway and waves. This level of agreement supports further investigations, as outlined in Table 8, which extend the analysed wave frequency range downward from 0.700 Hz to 0.450 Hz and include a broader set of leeway angles (0°, 2.5°, 5°, 7.5°, and 10°).

Table 8
The outline of the regular wave condition CFD analysis.

Wave frequency (ω) [Hz]	Wave period (T_m) [s]	Encountering wave period (T_e) [s]		Wavelength (λ) [m]
		for Fr 0.194	for Fr 0.246	
0.450	2.222	1.721	1.621	7.710
0.500	2.000	1.511	1.416	6.245
0.550	1.818	1.340	1.251	5.161
0.600	1.667	1.200	1.115	4.337
0.650	1.538	1.083	1.001	3.695
0.700	1.429	0.983	0.906	3.186
0.732	1.366	0.927	0.852	2.914
0.750	1.333	0.897	0.824	2.776
0.768	1.302	0.869	0.797	2.647
0.858	1.166	0.749	0.682	2.121
1.086	0.921	0.540	0.486	1.324

For any given leeway angle, the total resistance is consistently higher in waves than in calm water (Fig. 9), demonstrating the presence of wave-induced added resistance. In both calm water and waves, resistance increases with leeway angle, with the effect becoming more pronounced at larger angles (e.g., from 5° to 10°). Wave frequency also has a marked influence: for many leeway angles, resistance rises as frequency decreases from 1.086 Hz, reaching a peak around 0.600 Hz, before diminishing at higher frequencies. This highlights the critical role of wave conditions within the 0.550–0.650 Hz range at this Froude number. Calm-water resistance values provide benchmarks for each leeway angle, enabling direct comparison. Overall, the increase in resistance due to waves depends on both leeway angle and wave frequency, with the most pronounced added resistance occurring within the peak period (0.550–0.650 Hz) and at higher leeway angles. Consequently, the maximum total resistance in the examined range is

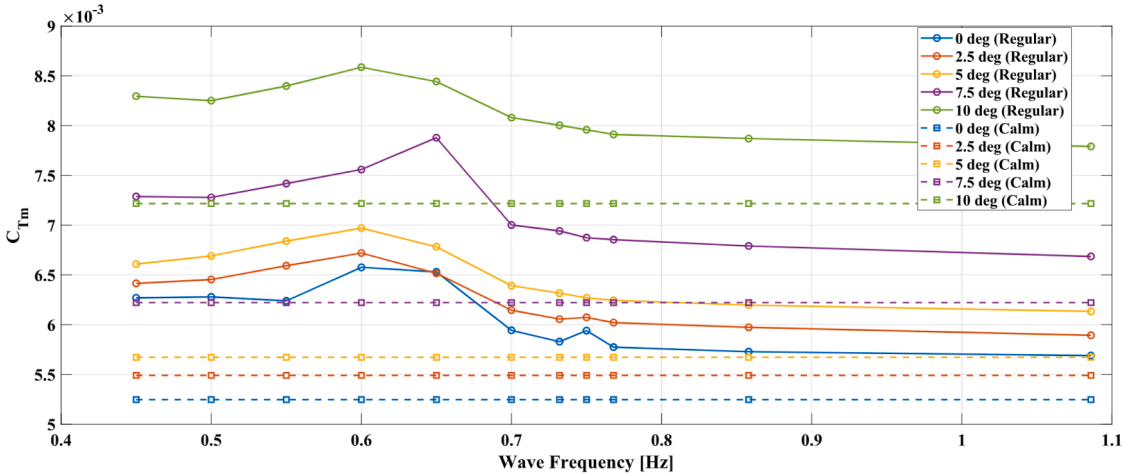

Fig. 9. C_{Tm} values of the model ship for various leeway angles in regular waves and calm water at $Fr = 0.194$.

observed at a leeway angle of 10° and a wave frequency of 0.600 Hz.

To evaluate the non-linear coupling between leeway and wave effects, a superposition analysis was conducted. As shown in Table 9, for the case with Fr = 0.194 at a wave frequency of 0.600 Hz, the increase in resistance coefficient due to leeway alone (0.0019705) and due to waves alone (0.0013290) sums to 0.0032995. In contrast, the resistance coefficient increases measured under the combined wave–leeway condition is 0.0033390, which is approximately 1.2% higher than the linear superposition. This synergistic effect is attributed to modifications in the pressure field and enhanced wave generation on the leeward side of the hull, as evidenced by the asymmetric free-surface patterns shown in Fig. 13. These results indicate that neglecting the coupled effects of leeway and waves can lead to an underestimation of the total resistance experienced by vessels operating under wind-assisted propulsion conditions in realistic sea states.

Fig. 10 presents the total resistance in both regular wave and calm-water conditions at a velocity corresponding to $Fr = 0.246$. The overall trend is similar to that observed at $Fr = 0.194$; however, the absolute resistance values increase with the higher velocity.

Fig. 11 illustrates the behaviour of the added resistance coefficient due to waves (σ_{AW}) as a function of the non-dimensional wavelength (λ/Lwl). Results are shown for five leeway angles (β; 0°, 2.5°, 5°, 7.5°, and 10°) at a constant speed corresponding to $Fr = 0.194$. Across all cases, σ_{AW} increases with wavelength, reaching a peak when $\lambda/Lwl \approx 1.6$), and then decreases as the relative wavelength becomes larger. Increasing the leeway angle generally (except for 2.5° leeway) yields higher σ_{AW} values over most of the examined wavelength range, with the effect being most pronounced near the peak region and at shorter wavelengths. When a vessel moves with a small leeway angle, as concluded in this research for the 2.5° leeway angle, the flow of water around the hull is slightly asymmetric, which may lead to a beneficial modification of the pressure field and wave system, particularly in the presence of head waves. Moreover, for the longer waves ($\lambda/Lwl > 1.6$), σ_{AW} decreases and the influence of leeway angle diminishes, as indicated by the convergence of the curves.

Fig. 12 shows the added resistance coefficient due to waves at a higher velocity corresponding to $Fr = 0.246$. While the general trend—an increase from shorter wavelengths, a peak, and a subsequent decrease in longer waves—mirrors the lower-speed condition, several distinctions are evident. At this speed, the maximum σ_{AW} shifts to a slightly higher wavelength ratio ($\lambda/Lwl \approx 1.7$) and its peak value is marginally lower than that observed at $Fr = 0.194$. As with the lower Froude number, increasing the leeway angle leads to consistently higher σ_{AW} values across most wavelengths. A notable feature at $Fr = 0.246$ is the appearance of a local minimum around $\lambda/Lwl \approx 1.1$. For longer waves ($\lambda/Lwl > 1.7$), the influence of leeway angle diminishes, with the curves converging in a manner similar to the $Fr = 0.194$ results.

Fig. 13 provides a visual comparison of the free-surface wave patterns generated by the model ship's hull at five leeway angles. Contour lines represent wave elevations, mapping both the diverging and transverse wave systems. At zero leeway, the wave pattern remains largely symmetrical; however, increasing the leeway angle introduces marked asymmetry, visible both in the near-hull region and in the far-field wake. The disturbance, particularly the divergent waves, intensifies on the side toward which the hull drifts. This visual evidence aligns with the quantitative results in Figs. 11 and 12, which demonstrate that higher leeway angles lead to greater energy transfer into wave generation and correspondingly higher σ_{AW} values. Moreover, analysing the ship's overall hydrodynamic behaviour requires consideration of both the amplitude (first-order harmonics) and average (zeroth-order harmonics) of its motions over a defined time period, as summarised in Table 10.

It is important to note that the observed increase in σ_{AW} arises from the combined effects of oblique wave incidence and leeway-induced flow asymmetry. While changes in the wave encounter angle modify wave reflection patterns, a non-zero leeway angle (β) significantly alters the mean hydrodynamic pressure distribution and generates a quasi-lift force. This behaviour is reflected in the systematic increase of the zeroth-order heave component and the pronounced asymmetry observed in the near-field wake. The results indicate that leeway introduces a synergistic increase in resistance that exceeds the linear superposition of its individual contributions, underscoring the importance of accounting for coupled leeway–wave interactions when assessing the performance of vessels equipped with wind-assisted propulsion systems.

Fig. 14 illustrates the vessel's periodic pitch and heave motions, both exhibiting a uniform cycle period of 1.2 s over the 6 s analysis interval (the last 5 encountering wave periods). A clear phase relationship is evident: the peak pitch angle occurs slightly before the maximum upward heave. The results indicate that the leeway angle has little influence on the oscillation amplitudes of pitch and heave. Similarly, the zeroth-order component of the pitch motion remains nearly constant across all leeway cases. In contrast, the most notable effect of increasing

Table 9
Values for the synergistic effect calculation for 0.600 Hz at $Fr = 0.194$.

Scenarios	Resistance coefficient [C_{Tm}]	Increase value for C_{Tm}
Calm water, $\beta = 0°$	0.0052468	-
Calm water, $\beta = 10°$	0.0072173	0.0019705
Regular wave, $\beta = 0°$	0.0065758	0.0013290
Regular wave, $\beta = 10°$	0.0085858	0.0033390

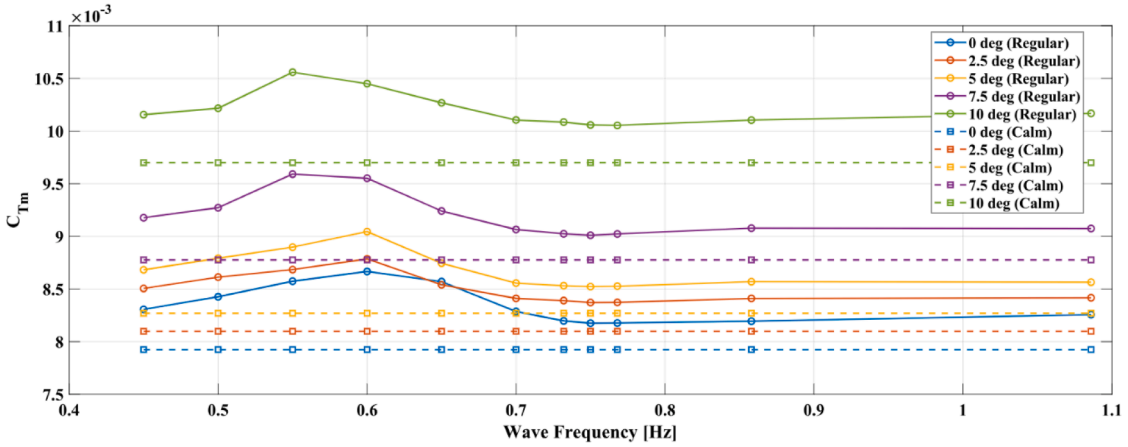

Fig. 10. C_{Tm} values of the model ship for various leeway angles in regular waves and calm water at $Fr = 0.246$.

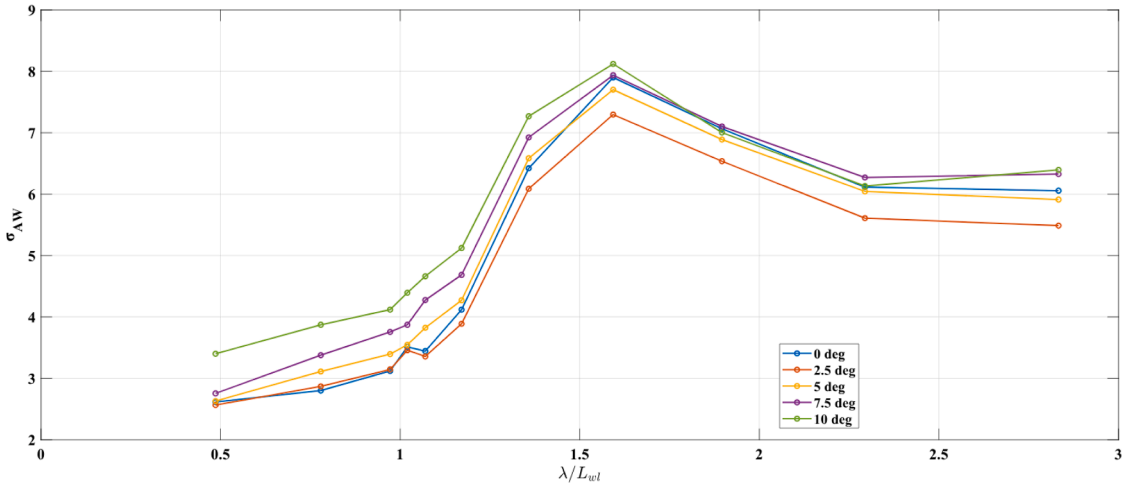

Fig. 11. The effect of leeway angle on the σ_{AW} for different λ/Lwl ratios at $Fr = 0.194$.

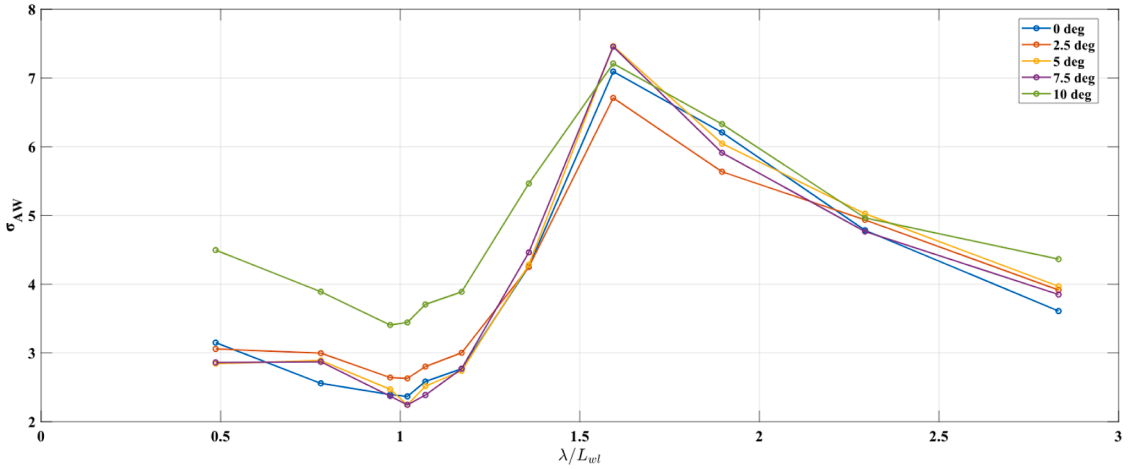

Fig. 12. The effect of leeway angle on the σ_{AW} for different λ/Lwl ratios at $Fr = 0.246$.

the leeway angle is a consistent rise in the zeroth-order heave component. This steady increase, independent of the first-order oscillations, is attributed to changes in the mean hydrodynamic pressure distribution around the hull. As the vessel assumes a leeway angle, the asymmetric flow generates a quasi-lift force that alters mean sinkage, effectively raising the hull in the water without significantly affecting its dynamic response to incident waves. Notably, the heave motion exhibits a negative zeroth-order component even at 0° leeway, suggesting that under these conditions the hull submerges below the design waterline on average.

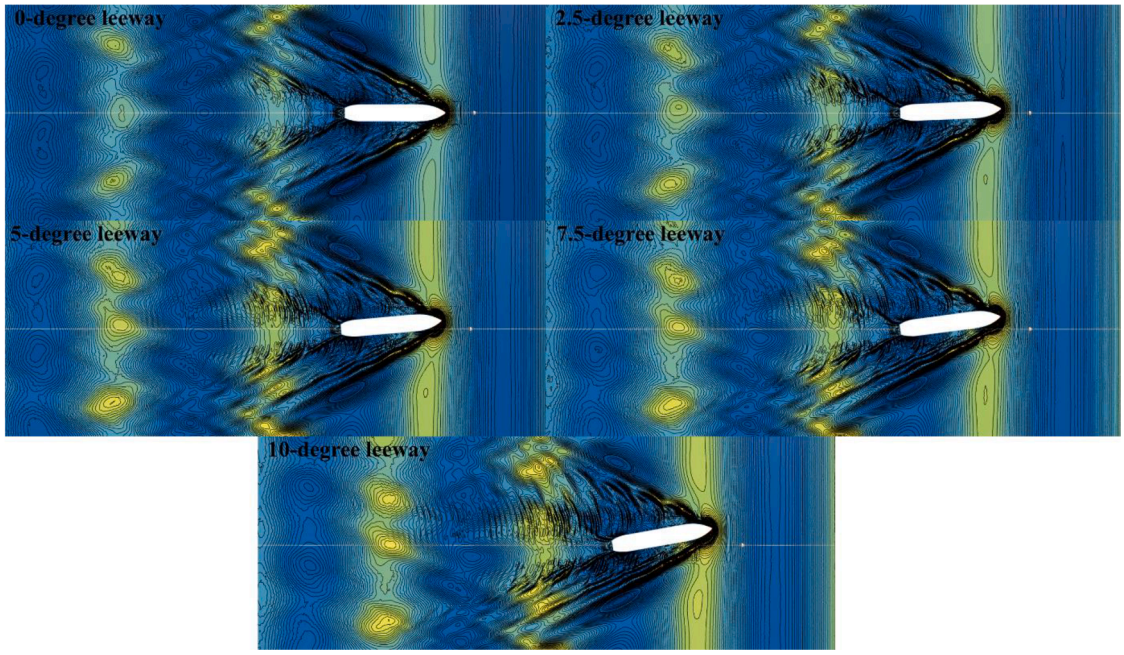

Fig. 13. Free surface formation for the 0.600 Hz wave frequency at a *Fr* of 0.194.

Table 10
Zeroth- and first-order harmonic components of pitch and heave motions under regular waves at 0.600 Hz and $Fr = 0.194$.

Leeway angles	Heave [mm]		Pitch (θ) [deg.]	
	1st order harmonics	0th order harmonics	1st order harmonics	0th order harmonics
0°	30.3	−5.06	0.325	0.161
2.5°	31.8	−5.13	0.305	0.150
5°	32.0	−5.48	0.321	0.159
7.5°	32.1	−6.03	0.343	0.172
10°	32.1	−6.79	0.370	0.186

Fig. 15 presents the wave cuts taken from three transverse positions on both the port and starboard sides of the model at five leeway angles (β) for $Fr = 0.246$ under regular waves of 0.600 Hz. The measure B denotes the model's beam, with positive values representing the port side and negative values the starboard. A section offset by one beam width to port from the centreline is designated as the "+B section". The rudder axis is located at x = 0 m, with the bow pointing in the +x direction. The vertical coordinate system is defined relative to the global reference frame, with z = 0 m corresponding to the keel line. In these simulations, the model draught was fixed at 0.17 m, and a positive leeway angle indicates drift toward port.

The results in Fig. 15 show that increasing the leeway angle amplifies wave magnitudes on the port side bow region, where the flow is influenced by both incident and ship-generated waves. By contrast, on the starboard side, the wave magnitudes are comparatively smaller, and in fact decrease with leeway angle, as this side is unaffected by the superimposed wave effect. With increasing transverse distance (from B to 2B), this asymmetry diminishes, and both sides exhibit more similar wave characteristics. The forward motion of the model in regular waves produces a pronounced bow wave, where first fluid contact occurs, governed by the hull geometry and orientation. The modification of the wave field due to leeway is most significant within the near- and mid-wake, extending approximately one ship length downstream; beyond this region, the effect of leeway angle on wave formation becomes minimal.

Fig. 16 illustrates the relationship between the angle β and the corresponding residual (unstable or imbalanced quantity in CFD) yawing

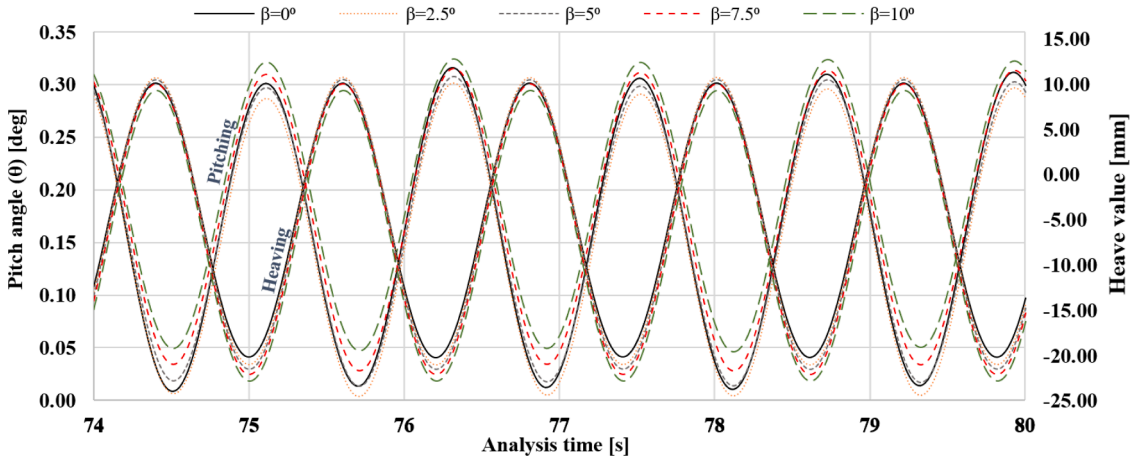

Fig. 14. Pitch and heave motions' time series of the 0.600 Hz regular wave condition for various leeway angles at a *Fr* of 0.194.

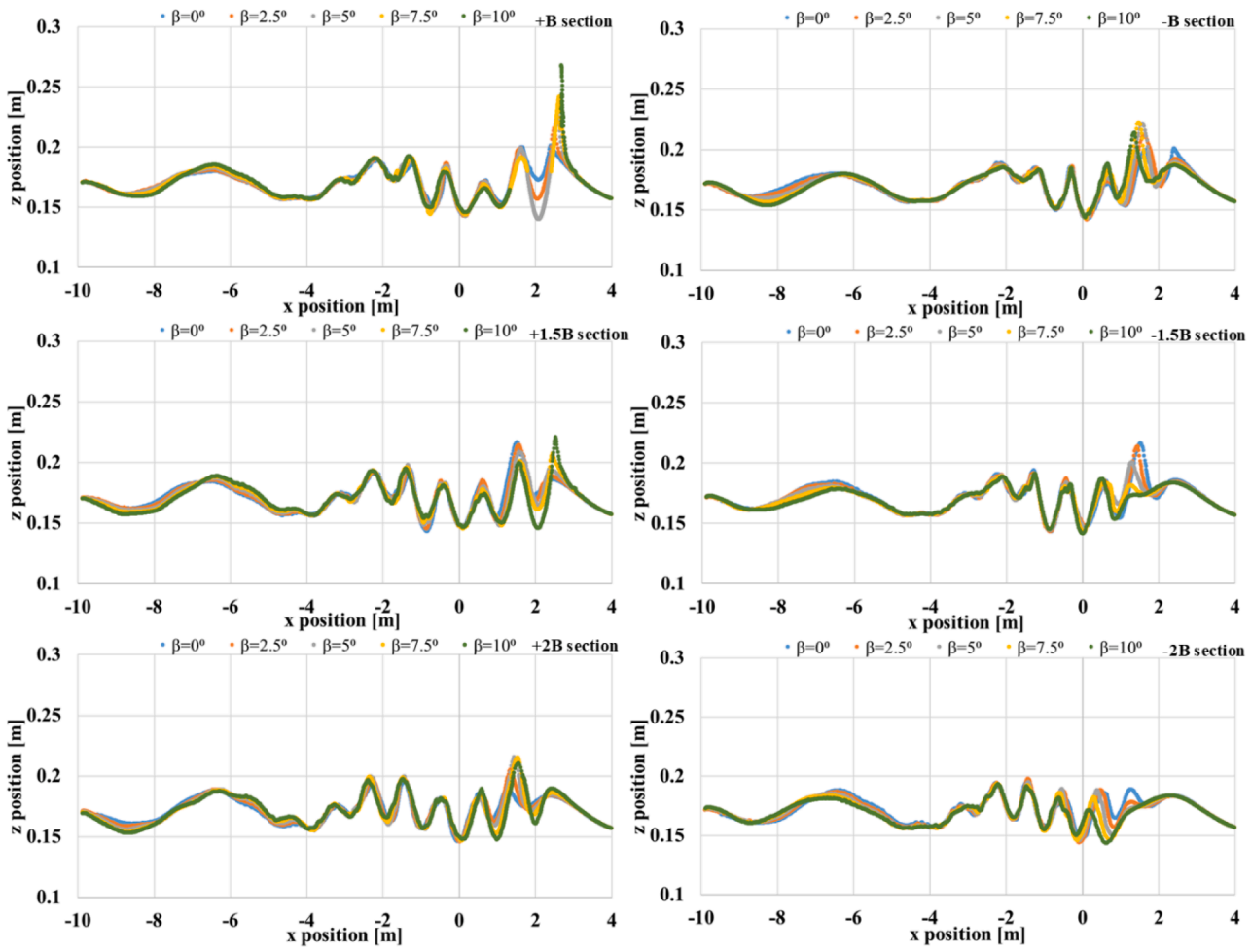

Fig. 15. Wave cuts at different sections for a 0.600 Hz wave frequency and $Fr = 0.246$.

moment coefficient (N'), calculated over the last 5 encountering wave periods. A remarkable observation is that for all non-zero values of β, the N' has a distinct and regular periodic oscillation, similar to a sinusoidal pattern, with a wave period of 1.2 s. The value of the β substantially affects the magnitudes of the residual yawing moment. As β increases, both the first-order and zeroth-order harmonics of the yawing moment coefficient significantly increase. At $\beta = 0°$, N' remains close to 0, as expected under symmetrical flow, though this may also reflect a baseline level of numerical uncertainty. As β increases, both the zeroth-order and first-order harmonic components of N' rise significantly. Specifically, at $\beta = 2.5°$, N' fluctuates between 0 and 0.01; at $\beta = 5°$, between 0.005 and 0.025; at $\beta = 7.5°$, between 0.005 and 0.035; and at $\beta = 10°$, between approximately 0.005 and 0.050. At this maximum angle, the zeroth-order harmonic is ~0.027, while the first-order harmonic reaches ~0.040. Across all non-zero β cases, the residual yawing moment is predominantly oriented in the +z direction, indicating a consistent

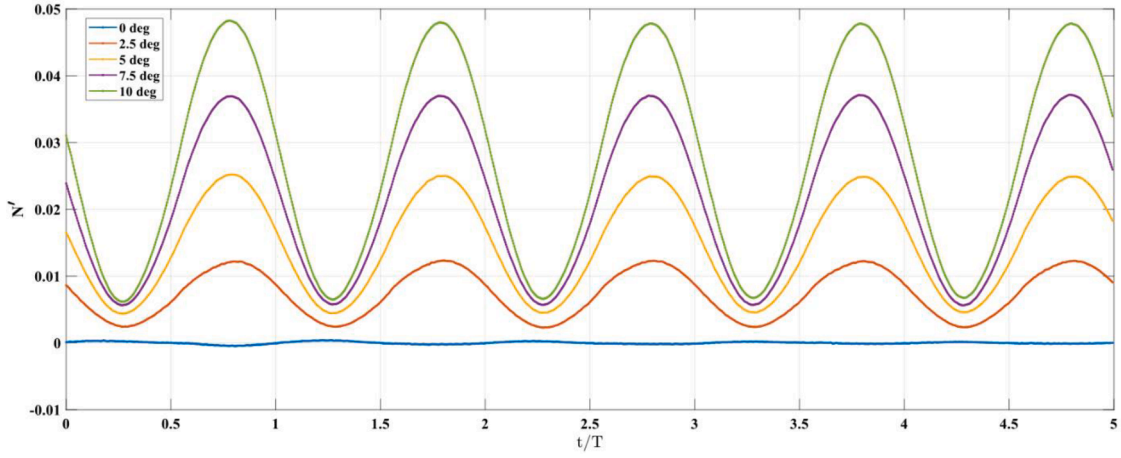

Fig. 16. Residual yawing moment coefficients for a 0.600 Hz wave frequency at $Fr = 0.194$.

tendency for portside rotation, though with varying magnitude depending on leeway angle.

Fig. 17 presents the residual rolling moment coefficient (K') over the last 5 encountering wave periods, classified by leeway angle β. The results reveal a clear positive correlation between β and K'. At $\beta = 0°$, K' remains close to zero, as expected under symmetrical flow. For non-zero leeway angles, K' exhibits a periodic oscillatory response whose magnitude increases substantially with β. At $\beta = 2.5°$, fluctuations range approximately from –0.02 to +0.02, while at $\beta = 10°$, the range expands significantly from about –0.08 to +0.11. These results highlight that increasing leeway induces progressively larger rolling moments, with well-defined periodicity evident across all non-zero β cases.

Finally, this study offers important quantitative data on relevant leeway-wave interactions; yet, it is important to understand the particular scope and limitations of the research. The study primarily focused on incident head waves, which simplify the stochastic and directionally distributed properties of real wave conditions. Moreover, assuming a constant rudder angle (0°) disregards the dynamic effects of steering systems. To improve environmental realism and the applicability of the findings, future studies should overcome these limitations by investigating scenarios with irregular waves and various wave directions (e.g., oblique and beam waves). Including the dynamic influence of the rudder would help to fully evaluate ship motions and total resistance. Investigating the responses of various hull forms to these coupled forces presents significant potential for future research. Adhering to these recommendations is crucial for improving performance prediction techniques and thereby promoting energy efficiency in vessel design and operation in the maritime industry.

5. Conclusions

This study examines the relationship between a ship's leeway angle and the frequency of the regular waves it encounters. The objective of the work was to quantify the combined impact of these factors on the added wave resistance experienced by the investigated vessel. A numerical methodology was developed to evaluate the vessel's hydrodynamic behaviour under various operating conditions through comparison of CFD simulations with EFD measurements.

To assess the numerical reliability of the CFD model, a verification study was conducted. The estimated order of accuracy (p) was conservatively limited to its theoretical value of 2.0, in accordance with the procedures proposed by Eça and Hoekstra (2009), to ensure a robust estimation of numerical uncertainty. The results indicate that, within the investigated refinement range, grid resolution has a greater influence on numerical uncertainty than time-step size. The numerical solutions are shown to be well converged and effectively independent of the spatial and temporal resolutions employed, as evidenced by GCI values remaining at approximately 1%, even after the conservative adjustment of the accuracy order.

The results indicate that the total resistance of the vessel increases consistently in both calm water and regular wave conditions when the vessel is operated with a non-zero leeway angle ($\beta \neq 0^o$) compared to operation at zero leeway angle ($\beta = 0^o$). This study additionally quantifies the substantial influence of the leeway angle on the added wave resistance coefficient (σ_{AW}). A peak in σ_{AW} was consistently observed when the wavelength (λ) was normalized by waterline length (Lwl) to a range of approximately $\lambda/Lwl \approx 1.6 - 1.7$. This range is frequently associated with resonant pitch and heave responses. The systematic increase of σ_{AW} across the majority of the wavelengths analysed was a critical finding related to head seas and increasing β. This increase was most pronounced in the shorter wave spectrum ($\lambda/Lwl < 1$) and near the aforementioned maximal resistance wavelength. Visualizations of the free surface wave patterns corroborated these quantitative results by demonstrating an increase in wake asymmetry and more energetic wave generation, particularly on the leeward side, as β increased. This observation is consistent with higher resistance and greater energy dissipation. Although β was discovered to have a substantial impact on the vessel's zeroth-order harmonics of the heave motion, which may be attributed to changes in the effective submerged geometry and hydrodynamic pressure distribution, its impact on pitch and heave motions' first-order harmonics was less pronounced within the scope of this investigation. Furthermore, the magnitude and fluctuating properties of the residual yawing and rolling moments were affected by the β, which significantly influences their magnitude. The consistent in-phase oscillations, with amplitudes directly related to β for non-zero moment values, emphasize its substantial impact on the monitored dynamics. These results have direct implications for the development of course-keeping algorithms and control strategies, providing crucial insights into the system's behaviour under various drift conditions.

The findings of this study highlight the critical importance of accounting for leeway angle dynamics in ship hydrodynamic assessments, particularly when evaluating the performance and fuel consumption of vessels equipped with Wind-Assisted Propulsion Systems. Such systems inherently generate side forces that often result in non-zero leeway angles during operation. The interaction between leeway-induced flow asymmetry and wave-induced phenomena produces a synergistic increase in resistance, which is significantly greater than the simple sum of calm-water leeway resistance and wave-added resistance at zero leeway. Neglecting this coupled effect risks a substantial underestimation of propulsion requirements and fuel consumption in realistic operating conditions where both waves and leeway are present.

The synergistic increase in resistance resulting from the interaction

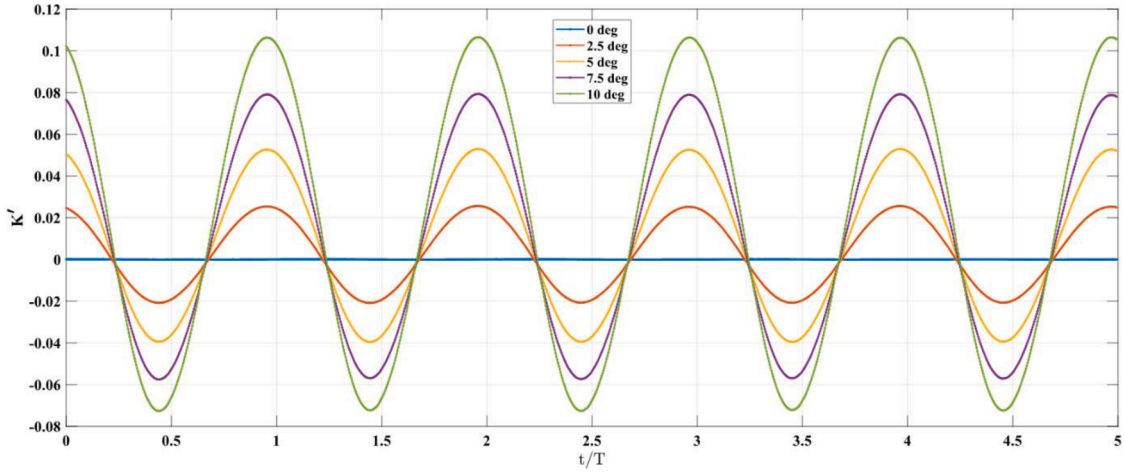

Fig. 17. Residual rolling moment coefficients for a 0.600 Hz wave frequency at $Fr = 0.194$.

between leeway-induced flow asymmetry and wave-induced phenomena exceeds the simple linear superposition of calm-water leeway resistance and wave-added resistance at zero leeway. For example, under combined conditions at a Froude number of 0.194 and a wave frequency of 0.600 Hz, the measured resistance increase was 1.2% greater than the sum of the individual contributions. This non-linear increment is attributed to amplified wave generation and a modified pressure distribution on the leeward side of the vessel. Under realistic operating conditions, where waves and leeway occur simultaneously, neglecting this coupled effect may therefore lead to an underestimation of propulsion requirements and associated fuel consumption.

It is also acknowledged that a non-zero leeway angle induces a rolling moment. In the present study, this effect was not captured, as only heave and pitch motions were released in order to isolate the primary vertical responses. Constraining the roll degree of freedom represents a methodological limitation, since allowing roll motion could further modify the effective submerged geometry and the associated added resistance characteristics. Consequently, future studies should consider employing a three-degree-of-freedom model to enable a more comprehensive assessment of vessel dynamic performance under drift conditions.

CRediT authorship contribution statement

Burak Göksu: Writing – original draft, Visualization, Software, Methodology, Investigation, Data curation, Conceptualization. **Suraj Garad:** Writing – review & editing, Validation, Resources, Data curation. **Stefano Pandini:** Resources, Project administration, Funding acquisition. **Edoardo Sirolla:** Resources, Project administration, Funding acquisition. **Robert Palin:** Resources, Project administration, Funding acquisition. **Nicholas Townsend:** Writing – review & editing, Resources, Project administration, Funding acquisition, Data curation. **Tahsin Tezdogan:** Writing – review & editing, Validation, Supervision, Resources, Project administration, Funding acquisition, Formal analysis.

Declaration of competing interest

The authors declare that they have no known competing financial interests or personal relationships that could have appeared to influence the work reported in this paper.

Acknowledgments

The study presented in this paper was carried out under the research project: Supercharging Wind Propulsion: Advancing Digital Tools in Maritime to Deliver Real-World Performance in a Next-Generation Wind Propulsion Design (Project Number: 10093454). This project is part of the Clean Maritime Demonstration Competition Round 4 (CMDC4), funded by the UK Department for Transport (DfT) and delivered by Innovate UK. CMDC4 is part of the Department's UK Shipping Office for Reducing Emissions (UK SHORE) programme, a £206 m initiative focused on developing the technology necessary to decarbonise the UK domestic maritime sector. The authors would like to acknowledge the support provided by Scotline Ltd. for their valuable contributions to this research.

References

Cairns, J., Vezza, M., Green, R., MacVicar, D., 2021. Numerical optimisation of a ship wind-assisted propulsion system using blowing and suction over a range of wind conditions. Ocean Eng. 240, 109903. https://doi.org/10.1016/j.oceaneng.2021.109903.

Čalić, A., Jurić, Z., Katalinić, M., 2024. Impact of wind-assisted propulsion on fuel savings and propeller efficiency: a case study. J. Mar. Sci. Eng. 12, 2100. https://doi.org/10.3390/jmse12112100.

Carrica, P.M., Fu, H., Stern, F., 2011. Computations of self-propulsion free to sink and trim and of motions in head waves of the KRISO container ship (KCS) model. Appl. Ocean Res. 33, 309–320. https://doi.org/10.1016/j.apor.2011.07.003.

CD-Adapco, 2023. Simcenter STAR-CCM+ 2306 user guide.

Celik, I.B., Ghia, U., Roache, P.J., Freitas, C.J., Coleman, H., Raad, P.E., 2008. Procedure for estimation and reporting of uncertainty due to discretization in CFD applications. J. Fluids Eng. ASME 130. https://doi.org/10.1115/1.2960953.

Cepowski, T., 2024. Utilizing artificial neural network ensembles for ship design optimization to reduce added wave resistance and CO2 emissions. Energies 17, 5326. https://doi.org/10.3390/en17215326.

Chen, S., Hino, T., Ma, N., Gu, X., 2018. RANS investigation of influence of wave steepness on ship motions and added resistance in regular waves. J. Mar. Sci. Technol. 23, 991–1003. https://doi.org/10.1007/s00773-018-0527-5.

Degiuli, N., Martić, I., Farkas, A., 2019. Environmental aspects of total resistance of container ship in the north atlantic. J. Sustain. Dev. Energy, Water Environ. Syst. 7, 641–655. https://doi.org/10.13044/j.sdewes.d7.0267.

Eça, L., Hoekstra, M., 2009. Evaluation of numerical error estimation based on grid refinement studies with the method of the manufactured solutions. Comput. Fluids 38, 1580–1591. https://doi.org/10.1016/j.compfluid.2009.01.003.

Gao, Q., Song, L., Yao, J., 2021. RANS prediction of wave-induced ship motions, and steady wave forces and moments in regular waves. J. Mar. Sci. Eng. 9, 1459. https://doi.org/10.3390/jmse9121459.

Garad, S., Townsend, N., Goksu, B., Tezdogan, T., 2024. CMDC4: super charging wind propulsion model scale experimental results v3.0 (confidential). Southampton.

Göksu, B., Garad, S., Pandini, S., Sirolla, E., Palin, R., Townsend, N., Tezdogan, T., 2025. Impact of leeway and rudder angles on ship resistance: a numerical planar motion mechanism approach. Ocean Eng. 338, 121952. https://doi.org/10.1016/j.oceaneng.2025.121952.

Guerri, O., Liberge, E., Hamdouni, A., 2016. Numerical simulation of the turbulent flow around an oval-sail. J. Appl. Fluid Mech. 9, 2009–2023. https://doi.org/10.18869/acadpub.jafm.68.235.24117.

Holtrop, J., Mennen, G.G.J., 1982. An approximate power prediction method. Int. Shipbuild. Prog. 29, 166–170.

Huang, L., Song, Q., Zhang, R., Wang, K., Ma, R., 2023. Study of the influence of rotor shape on the aerodynamic characteristics of flettner rotor. Advances in machinery, materials science and engineering application IX. IOS Press, pp. 798–804. https://doi.org/10.3233/ATDE230543.

IMO, 2023. Improving the energy efficiency of ships [www document].

Inal, O.B., Charpentier, J.F., Deniz, C., 2022. Hybrid power and propulsion systems for ships: current status and future challenges. Renew. Sustain. Energy Rev. 156, 111965. https://doi.org/10.1016/j.rser.2021.111965.

ITTC, 2024. ITTC – recommended procedures and guidelines uncertainty analysis for manoeuvring predictions based on captive manoeuvring tests.

ITTC, 2021a. ITTC – recommended procedures and guidelines resistance test, ITTC – recommended procedures and guidelines.

ITTC, 2021b. ITTC-recommended procedures and guidelines uncertainty analysis in CFD verification and validation methodology and procedures [www document]. URL. https://www.ittc.info/media/9765/75-03-01-01.pdf (accessed 6.12.24).

ITTC, 2014. 7.5-03-02-03 practical guidelines for ship CFD applications, ITTC – recommended procedures and guidelines.

ITTC, 2011. 7.5-03-02-03 practical guidelines for ship CFD applications, ITTC – recommended procedures and guidelines.

Jawa, S., Munehiko, M., 2023. Validation of short-term prediction of added resistance in head seas considering wave steepness nonlinearity with probability density function method. Ocean Eng. 278, 114353. https://doi.org/10.1016/j.oceaneng.2023.114353.

Jimenez, V.J., Kim, H., Munim, Z.H., 2022. A review of ship energy efficiency research and directions towards emission reduction in the maritime industry. J. Clean. Prod. 366, 132888. https://doi.org/10.1016/j.jclepro.2022.132888.

Julià, E., Tillig, F., Ringsberg, J.W., 2020. Concept design and performance evaluation of a fossil-free operated cargo ship with unlimited range. Sustainability 12, 6609. https://doi.org/10.3390/su12166609.

Khan, L., Macklin, J., Peck, B., Morton, O., Souppez, J.B.R., 2021. A review of wind-assisted ship propulsion for sustainable commercial shipping: latest developments and future stakes. In: Wind Propulsion Conference. Royal Institution of Naval Architects.

Kim, D., Song, S., Jeong, B., Tezdogan, T., 2021. Numerical evaluation of a ship's manoeuvrability and course keeping control under various wave conditions using CFD. Ocean Eng. 237, 109615. https://doi.org/10.1016/j.oceaneng.2021.109615.

Kim, M., Hizir, O., Turan, O., Day, S., Incecik, A., 2017. Estimation of added resistance and ship speed loss in a seaway. Ocean Eng. 141, 465–476. https://doi.org/10.1016/j.oceaneng.2017.06.051.

Klein, M., Dudek, M., Clauss, G.F., Ehlers, S., Behrendt, J., Hoffmann, N., Onorato, M., 2020. On the deterministic prediction of water waves. Fluids 5, 9. https://doi.org/10.3390/fluids5010009.

Lee, S.H., Paik, K.J., Lee, J.H., 2022. A study on ship performance in waves using a RANS solver, part 2: comparison of added resistance performance in various regular and irregular waves. Ocean Eng. 263, 112174. https://doi.org/10.1016/j.oceaneng.2022.112174.

Liu, S., Song, J., Zhang, L., Tan, Y., 2024. Adaptive finite-time backstepping integral sliding mode control of three-degree-of-freedom stabilized system for ship propulsion-assisted sail based on the inverse system method. J. Mar. Sci. Eng. 12, 348. https://doi.org/10.3390/jmse12020348.

Martić, I., Degiuli, N., Farkas, A., Gospić, I., 2020. Evaluation of the effect of container ship characteristics on added resistance in waves. J. Mar. Sci. Eng. 8, 696. https://doi.org/10.3390/JMSE8090696.

Pan, P., Sun, Y., Yuan, C., Yan, X., Tang, X., 2021. Research progress on ship power systems integrated with new energy sources: a review. Renew. Sustain. Energy Rev. 144, 111048. https://doi.org/10.1016/j.rser.2021.111048.

Plessas, T., Papanikolaou, A., 2024. Optimization of ship design for the effect of wind propulsion. In: Proceedings of 15th international marine design conference (IMDC-2024). https://doi.org/10.3390/jmse13010167.

Saydam, A.Z., Kucuksu, G.N., Insel, M., Gokcay, S., 2022. Investigation of the influence of wind-assisted propulsion devices on hull design, in: sustainable development and innovations in marine technologies. pp. 211–216. https://doi.org/10.1201/9781003358961-27.

Seo, S., Park, S., Koo, B.Y., 2017. Effect of wave periods on added resistance and motions of a ship in head sea simulations. Ocean Eng. 137, 309–327. https://doi.org/10.1016/j.oceaneng.2017.04.009.

Söding, H., Shigunov, V., Schellin, T.E., El Moctar, O., 2014. A rankine panel method for added resistance of ships in waves. J. Offshore Mech. Arct. Eng. 136, 031601. https://doi.org/10.1115/1.4026847.

Stagonas, D., Higuera, P., Buldakov, E., 2018. Simulating breaking focused waves in CFD: methodology for controlled generation of first and second order. J. Waterw. Port, Coastal, Ocean Eng. 144, 06017005. https://doi.org/10.1061/(asce)ww.1943-5460.0000420.

Talluri, L., Nalianda, D.K., Kyprianidis, K.G., Nikolaidis, T., Pilidis, P., 2016. Techno economic and environmental assessment of wind assisted marine propulsion systems. Ocean Eng. 121, 301–311. https://doi.org/10.1016/j.oceaneng.2016.05.047.

Tezdogan, T., Demirel, Y.K., Kellett, P., Khorasanchi, M., Incecik, A., Turan, O., 2015. Full-scale unsteady RANS CFD simulations of ship behaviour and performance in head seas due to slow steaming. Ocean Eng. 97, 186–206. https://doi.org/10.1016/j.oceaneng.2015.01.011.

Vigna, V., Figari, M., 2023. Wind-assisted ship propulsion: matching flettner rotors with diesel engines and controllable pitch propellers. J. Mar. Sci. Eng. 11, 1072. https://doi.org/10.3390/jmse11051072.

Zhang, Y., Windén, B., Ojeda, H.R.D., Hudson, D., Turnock, S., 2024. Influence of drift angle on the propulsive efficiency of a fully appended container ship (KCS) using computational fluid dynamics. Ocean Eng. 292, 116537. https://doi.org/10.1016/j.oceaneng.2023.116537.